Applied Catalysis B: Environmental 254 (2019) 463–470

Contents lists available at ScienceDirect

Applied Catalysis B: Environmental

journal homepage: www.elsevier.com/locate/apcatb

# Selective photocatalytic conversion of alcohol to aldehydes by singlet oxygen over Bi-based metal-organic frameworks under UV–vis light irradiation

Ruoqian Zhang[a], Yuanyuan Liu[a,*], Zeyan Wang[a], Peng Wang[a], Zhaoke Zheng[a], Xiaoyan Qin[a], Xiaoyang Zhang[a], Ying Dai[b], Myung-Hwan Whangbo[a,c,d], Baibiao Huang[a,*]

[a] State Key Laboratory of Crystal Materials, Shandong University, Jinan 250100, China
[b] School of Physics, Shandong University, 250100, China
[c] Department of Chemistry, North Carolina State University, Raleigh, NC, 27695-8204, USA
[d] State Key Laboratory of Structural Chemistry, Fujian Institute of Research on the Structure of Matter (FJIRSM), Chinese Academy of Sciences (CAS), Fuzhou 350002, China

ARTICLE INFO

*Keywords:*
Excitons
Singlet oxygen
Bi-based MOFs
Photocatalysis
Selective oxidation

ABSTRACT

So far, most efforts in photocatalysis have been devoted to the separation of photogenerated electron-hole pairs, and possible use of excitons (i.e., electron-hole pairs) for photocatalytic processes has not received much attention. In this work, we studied the effect of metal dots on the excitonic behaviors of two bismuth-based MOFs, Bi-TATB and Bi-BTC (here the tridentate ligands $TATB^{3-}$ and $BTC^{3-}$ represent the carboxylates of 4,4′,4″-s-triazine-2,4,6-triyl-tribenzoic and 1,3,5-benzenetricarboxylic acids, respectively). The organic ligands (TATB and BTC) display different emission properties from the corresponding Bi based MOFs. Specifically, TATB and BTC display strong fluorescence emission while Bi-TATB and Bi-BTC display strong phosphorescence emission, suggesting the higher efficiency of intersystem crossing for Bi-TATB and Bi-BTC. The reason is attributed to the coordination with Bi, which promotes the singlet→ triplet intersystem crossing of the organic ligand due to the heavy metal effect. The enhanced triplet excited emission of Bi-TATB and Bi-BTC was further confirmed by the detection of $^1O_2$, as $^1O_2$ is well known to be formed due to energy transfer from the triplet state of photosensitizers to the ground-state oxygen ($^3O_2$). With above understanding, Bi-TATB and Bi-BTC were finally used to high selective photooxidation of benzyl alcohol to benzaldehyde. This work presents new understanding of the photophysical properties of Bi based MOFs, which provides alternative ideas on designing materials for selective photo-oxidation.

## 1. Introduction

As a novel and clean method to solve the energy crisis and environmental pollution, photocatalysis has been widely used in many ways, which includes photocatalytic hydrogen/oxygen production [1–5], degradation of organic pollutants [6], $CO_2$ reduction [7,8], and selective organic synthesis [9]. The species responsible for these photocatalytic reactions are electrons and holes separated from the photogenerated electron-hole pairs. Excitons, i.e., bound electron-hole pairs, play a critical role in light emitting devices [10,11], optoelectronic detectors [12], and solar cell devices [13,14], but have long been neglected in photocatalysis [15–20].

It was reported that there are two pathways for the subsequent reaction of charge carriers [21]. The first process is electron transfer (type I), which gives rise to reactive species like $^{\cdot}OH$, $O_2^{\cdot -}$, etc. This process is widely accepted as the mechanism for the photocatalytic degradation of organic molecules [22,23]. The second one is energy transfer process (type II) from triplet excitons to ground state oxygen ($^3O_2$) with singlet oxygen $^1O_2$ as the product. As can be seen, the formation of triplet excitons is a prerequisite for the $^1O_2$ production. Therefore, some organic dyes exhibiting large magnitude of triplet excitons were recognized as effective sensitizers for singlet oxygen $^1O_2$, such as porphyrins [24], phthalocyanines [25], polypyrrole macrocycles [26], chlorin [27] and their derivatives etc. The formation of triplet excitons in turn needs the intersystem crossing from excited singlet state to the triplet state. Heavy atom effect (HAE) was reported to promote the intersystem crossing due to the enhanced spin-orbital coupling [28].

Metal organic frameworks (MOFs) composed of heavy metal cations

* Corresponding authors.
*E-mail addresses:* yyliu@sdu.edu.cn (Y. Liu), bbhuang@sdu.edu.cn (B. Huang).

https://doi.org/10.1016/j.apcatb.2019.05.024
Received 23 January 2019; Received in revised form 24 April 2019; Accepted 5 May 2019
Available online 07 May 2019
0926-3373/ 

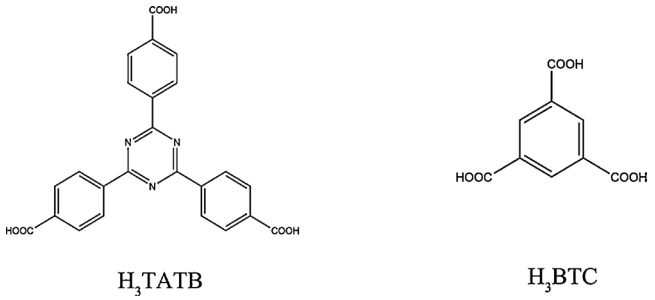


$H_3TATB$ $H_3BTC$

**Fig. 1.** Structures of $H_3TATB$ and $H_3BTC$.

and multidentate organic ligands are ideal structures in which organic molecules are maximally exposed to the heavy-atom effect. There are some reports about the energy transfer process of triplet excitons on MOFs [29–31], and some of them were applied to photodynamic therapy, which is a potential approach to cancer therapy. However, the choice of organic ligands is still concentrated on traditional porphyrins and the metals are limited to Zr [32–34], Hf [35,36], Gd [37] and some lanthanide metal [38]. It is of great significance to exploit other non-porphyrin based materials and enrich the MOFs systems as singlet oxygen $^1O_2$ sensitizers.

With that in mind, we choose the popular triazine and common phenyl carboxylic compound as the organic ligands and Bi as metal node. Bi-based inorganic compounds are widely used in photocatalysis and our group has demonstrated that some bismuth based MOFs possess photocatalytic properties [5,39]. In addition, the heavy atom effect of Bi has not been studied as far as we know. In this work, $Bi^{3+}$ cations and tridentate ligands such as $H_3TATB$ (4,4′,4″-s-triazine-2,4,6-triyl-tribenzoic acid) and $H_3BTC$ (1,3,5-benzenetricarboxylic acid) (Fig. 1) form Bi-MOFs, Bi-TATB [40] and Bi-BTC [39], respectively. Upon excitation, the tridentate ligands in these Bi-MOFs are expected to reach their triplet excited states due to the heavy atom effect of the $Bi^{3+}$ cations and hence induce the $^3O_2 \rightarrow {}^1O_2$ intersystem crossing. The generated singlet oxygen is used to oxidize alcohol to aldehydes which displays excellent selectivity. It is the first time to solve photocatalytic problems in MOFs with the conception of excitons and we also provide alternative materials to generate singlet oxygen without traditional porphyrins MOFs.

## 2. Experiment section

### 2.1. Synthesis of Bi-TATB

$H_3TATB$ (60.0 mg, 136.0 μmol) and $Bi(NO_3)_3{\cdot}5H_2O$ (57.4 mg, 118.4 μmol) were mixed in a mixture of DMF (6 mL) and MeOH (6 mL). After stirred for 30 min, the mixture was sealed in a 20 mL Teflon-lined autoclave, kept at 130℃ for 44 h and then cooled down to room temperature at normal speed. The solid product was filtered off and washed with DMF (20 mL) and MeOH (20 mL). A white powder was obtained and then dried in air at 60℃.

### 2.2. Synthesis of Bi-BTC

$Bi(NO_3)_3{\cdot}5H_2O$ (0.2360 g, 0.49 mmol) and $H_3BTC$ (0.1930 g, 0.92 mmol) were mixed in a mixture of DMF/MeOH (5 mL, 1:3). The solution was then sealed in a 100 mL Teflon-lined autoclave, heated to 120℃ for 45 h, kept at this temperature for 12 h and then cooled down slowly at the rate of 2℃/min to room temperature. Colorless crystals were washed by DMF, methanol and then dried in air at 60℃.

### 2.3. Molecular oxygen activation measurements

In a typical test, 4 mg catalyst was dispersed into 1 mL aqueous solution by ultrasonic process, then 200 μL catalyst solution was added into 20 mL TMB solution. TMB solution was prepared by using HAc/NaAc buffer solution (pH = 4.00) as solvent and the concentration of TMB was 500 μM. The mixture was illuminated with $O_2$ bubbling by using a xenon lamp (300 W) without cutoff filter as light source. The samples were taken at different time intervals for UV–vis measurements. The oxidation of TMB molecules was evaluated by monitoring the absorbance around 370 nm with a UV–vis spectrophotometer. The measurements were also performed under other gas environments (Ar and air). To verify the type of active oxygen species, different scavenger molecules were added into the solution prior to the UV–vis measurements: (1) carotene (20 mg); (2) mannite (50 mM, 1 mL); (3) catalase (4000 unit/mL, 1 mL); (4) superoxide dismutase (SOD, 5000 unit/mL, 1 mL).

### 2.4. Electron spin resonance trapping measurements

12 mg samples was dispersed into 3 mL acetone. Then 500 μL suspension of samples was mixed with 5 mL of 2,2,6,6-tetramethylpiperidine (TEMP, 50 mM) solution. The $O_2^{\cdot -}$ and $H_2O_2$ trapping-ESR tests were performed in methanol and double-distilled water, using 5,5-dimethyl-1-pyrroline-*N*-oxide (DMPO, 20 mM) as the spin-trapping agent. After being illuminated for 1.5 min ($H_3TATB$, Bi-TATB) or being illuminated for 7 min ($H_3BTC$, Bi-BTC), the mixture was characterized using a Bruker EMX plus model spectrometer operating at the X-band frequency (9.4 GHz) at room temperature. A xenon lamp (300 W) without cutoff filter was used as light source.

### 2.5. Alcohol photo-oxidation reactions

20 mg of Bi-TATB or Bi-BTC, 20 μmol of alcohol compounds, and 20 mL n-hexane were placed in a two-neck quartz reactors. The catalytic oxidation reaction was kept at constant temperature (~15 °C) with $O_2$ bubbling under irradiation with a 300 W Xe lamp (PLS-SXE300, Beijing Perfectlight Technology Co., LTD, China) without filter. The yield and type of the product was analyzed by GC–MS chromatography (GC-MS-QP2010, SH-Rtx-Wax column).

### 2.6. Characterizations methods

X-ray diffraction (XRD) characterizations were carried out on a Bruker AXS D8 with Cu Kα radiation (λ = 1.54178 Å). X-ray photoelectron spectroscopy (XPS) was performed on an ESCALAB MKII spectrometer. Scanning electron microscope (SEM) photograph was measured by Hitachi S-4800. The UV–vis diffuse reflectance spectra (DRS) were performed on a Shimadzu UV-2550 recording spectrophotometer, which was equipped with an integrating sphere and $BaSO_4$ was used as a reference. A Micromeritics ASAP 2020 analyzer was applied to measure the Brunauer-Emmet-Teller (BET) surface areas of the samples at liquid nitrogen temperature, and the activation process was carried out at 150 ℃ for 5 h in vacuum. The steady-state fluorescence spectra and phosphorescence spectra were collected on Hitachi F-7000 fluorescence spectrophotometer.

## 3. Results and discussion

Bi-BTC was synthesized according to previous literature [39]. Bi-TATB was obtained via a solvothermal reaction at 130 °C, which is slightly different from the preparation method reported in the literature [40]. The XRD profiles of the as-synthesized Bi-BTC and Bi-TATB are given in Figure S1 and Fig. 2a, which suggest that both of them were synthesized successfully. In Fig. 2a, the main peaks at 2θ = 6.6°, 8.6°and 11.3°, well match with the simulated results, and are in good accordance with the (210), (220) and (230) planes of Bi-TATB. The SEM images show Bi-BTC has an irregular bulk morphology (Figure S2), while Bi-TATB has a thick sheet morphology (Figure S3a). The

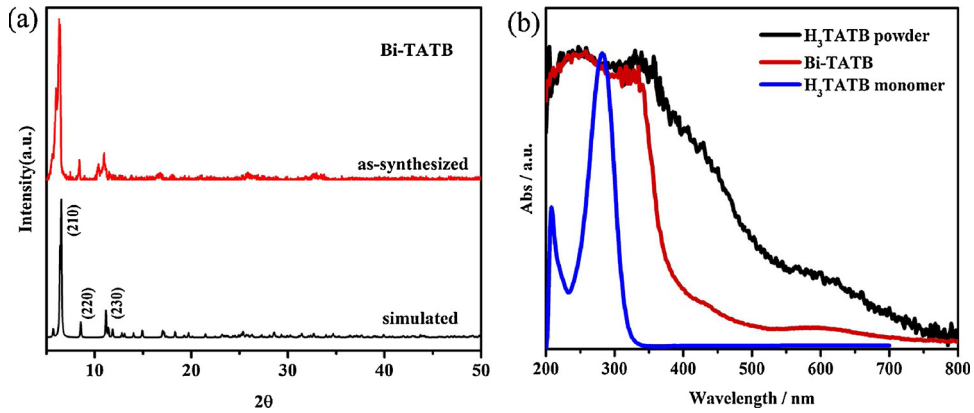


**Fig. 2.** (a) Observed and simulated XRD patterns of Bi-TATB. (b) Absorption spectra of the powder samples of $H_3$TATB and Bi-TATB as well as $H_3$TATB dissolved in aqueous NaOH solution (0.1 M).

corresponding elemental mapping further suggests that all elements (C, O, N and Bi) are uniformly distributed in Bi-TATB (Figure S3b-e). The XPS spectra of Bi-TATB displayed in Figure S3f show that it consists of C, O, N and Bi. Furthermore, no difference is observed between $H_3$TATB and Bi-TATB with respect to the N 1s XPS spectra, suggesting that Bi does not coordinate with the N in the triazine ring. (Figure S4a). In contrast, the fitting curves of the O 1s XPS spectra (Figure S4b) show two peaks for $H_3$TATB corresponding to the two different O atoms of a carboxyl group, -C(=O)OH, however, only one peak for Bi-TATB can be fitted, which indicates the coordination of $Bi^{3+}$ with a carboxylate oxygen of $TATB^{3-}$ in Bi-TATB.

The UV–vis absorption spectra measured for powder samples of $H_3$TATB and Bi-TATB are compared in Fig. 2b with those of $H_3$TATB molecules dissolved in aqueous NaOH solution in which $H_3$TATB exists as individual monomers. The absorption of $H_3$TATB powder has a broad shoulder at above ~412 nm and is red shifted from that of $H_3$TATB in solution (Fig. 2b). Such phenomenon is found for many planar molecules that aggregate by forming stacks of molecules in solid state [41]. The absorption edge of Bi-TATB, located at ~380 nm, is blue-shifted with respect to the broad shoulder in the absorption spectrum of $H_3$TATB powder. This indicates the absence of molecular stacking in Bi-TATB, as expected from the coordination of $TATB^{3-}$ with $Bi^{3+}$ to form the MOF structure. Such absorption shifts have been observed in the NU and MIL series (e.g., NU-901, NU-1000, $NH_2$-MIL-125) of MOFs [42,43]. Compared with the absorption spectrum of Bi-BTC with an absorption edge at ~313 nm (Figure S5), Bi-TATB has a stronger absorption intensity and a wider range of visible light absorption.

Photoluminescence behaviors of $H_3$TATB, Bi-TATB, $H_3$BTC and Bi-BTC were compared in Fig. 3. The steady-state fluorescence spectra of $H_3$TATB and Bi-TATB recorded at 293 K are shown in Fig. 3a, which reveals that both of them have a similar emission peak (~467 nm). However, Bi-TATB displays a much lower intensity than does $H_3$TATB. As the fluorescence arises from a radiative decay of singlet excitons [44], the lower intensity for Bi-TATB indicates that the population of the singlet excitons is lower. The time-resolved fluorescence spectra monitored at 467 nm (Fig. 3b) show that the average lifetime is slightly longer for $H_3$TATB than for Bi-TATB (~2.20 vs. ~2.05 ns). Fig. 3c compares the phosphorescence spectra of $H_3$TATB and Bi-TATB recorded at 77 K. Bi-TATB shows a strong phosphorescence emission peak at ~500 nm, exhibiting a red-shift with respect to the fluorescence peak at 467 nm. This red-shift clearly indicates the existence of long-lived triplet excitons. The long lifetime 4.77 ms of Bi-TATB (Fig. 3d) further confirms that the emission is due to the triplet excitons. In contrast, $H_3$TATB powder displays a very low emission in the visible light region of 500~600 nm and a small peak-like feature at 629 nm, which may be ascribed to an instrument noise due to its poor emission. The dramatic difference in the phosphorescence intensities between Bi-TATB and $H_3$TATB suggests that Bi-TATB produces much more triplet excitons than does $H_3$TATB. The lifetime 14.83 μs of $H_3$TATB further confirms the absence of triplet excitons in pure $H_3$TATB. Considering the aggregation of $H_3$TATB molecules in powder samples, similar experiments were carried out using $H_3$TATB monomers dissolved in NaOH solution. As shown in Figure S6a, the maximum emission of $H_3$TATB monomer is located at 429 nm with a shoulder at 313 nm. When the solvent is replaced with DMF, the emission peaks locate at 429 nm and 346 nm so that the peak at 429 nm should be ascribed to intrinsic emission of $H_3$TATB. The average lifetime for the $H_3$TATB monomer is determined to be ~4.59 ns (Figure S6b). The phosphorescence spectra of the $H_3$TATB monomer recorded at 77 K (Figure S6c) show that, at low temperature, the intrinsic emission is red-shifted to 465 nm with very low intensity. Combined with the short lifetime of 8.52 μs (Figure S6d), it is concluded that there is a small amount of triplet excitons in the $H_3$TATB monomer. The above results show that the production of triplet excitons in $H_3$TATB is really low regardless of $H_3$TATB molecules are aggregated or not. In Bi-TATB, the $TATB^{3-}$ ligand produces a large quantity of triplet excitons compared with $H_3$TATB, due most likely to the heavy-atom effect of the $Bi^{3+}$ cations. To test if this result is also applicable to other Bi-MOFs, we carried out similar experiments for $H_3$BTC and Bi-BTC. The steady-state fluorescence spectra of $H_3$BTC and Bi-BTC at room temperature have already been reported in the literature [39]. $H_3$BTC exhibits an intense emission at 410 nm, and Bi-BTC displays a red shift emission at 429 nm. The average lifetimes of $H_3$BTC and Bi-BTC monitored at their emission peaks at room temperature (Figure S7) are slightly different (~1.17 and ~1.16 ns, respectively). The phosphorescence spectra recorded at 77 K (Fig. 3e) reveal that Bi-BTC exhibits a strong phosphorescence emission peak at ~443 nm, which is red-shifted with respect to the fluorescence peak at 429 nm. In contrast, the phosphorescence intensity for $H_3$BTC is so weak that its emission peak overlaps the instrument noise completely. Similarly, its lifetime cannot be measured indicating that it has a really short lifetime. The long phosphorescence lifetime of Bi-BTC (2.87 ms) further confirms the existence of long-lived triplet excitons (Fig. 3f). Note that the lifetime of Bi-BTC is shorter than that of Bi-TATB (2.87 vs. 4.77 ms). This may have an important consequence on the oxidation experiments (see below).

Either for the $H_3$TATB aggregation powder, $H_3$TATB monomer or $H_3$BTC, the production of triplet excitons is negligible. While with the presence of Bi atom, triplet excitons are generated substantially. From above results, we can get the conclusion that for these Bi-MOFs, it is easier to reach their triplet excited states due to the heavy atom effect of the $Bi^{3+}$ cations.

Singlet oxygen $^1O_2$, a mild yet efficient oxidant [45], has proven to be a versatile reactive oxidizing species with applications in various organic transformations [46], fluorescent probe [47,48] and

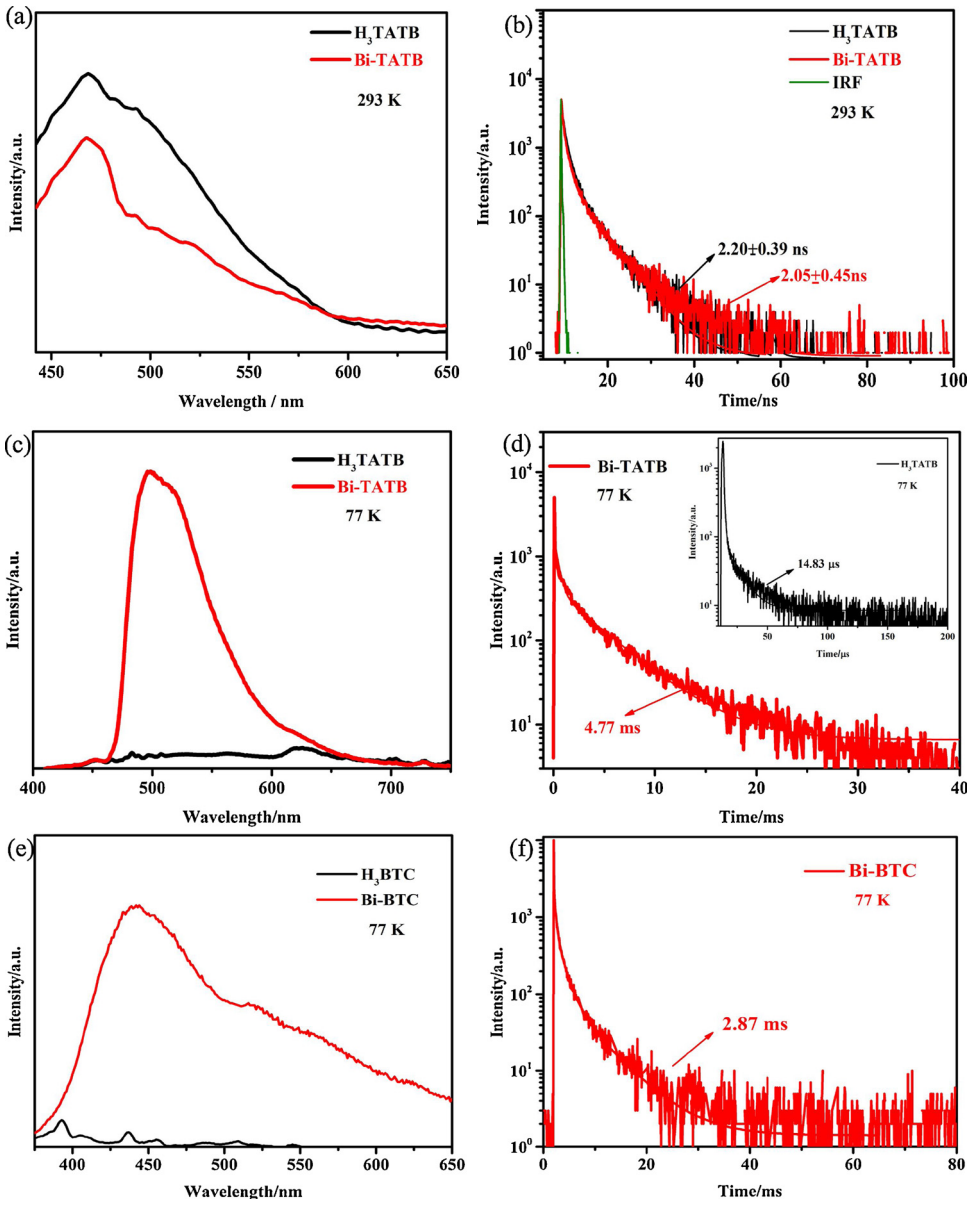


**Fig. 3.** (a) Steady-state fluorescence spectra of $H_3$TATB powder and Bi-TATB at 293 K. (b) Time-resolved fluorescence spectra of $H_3$TATB powder and Bi-TATB monitored at 467 nm at 293 K. (c) Phosphorescence spectra of $H_3$TATB powder and Bi-TATB at 77 K. (d) Time-resolved phosphorescence spectra of $H_3$TATB powder and Bi-TATB monitored at 500 nm at 77 K. (e) Phosphorescence spectra of $H_3$BTC powder and Bi-BTC at 77 K. (f) Time-resolved phosphorescence spectra of Bi-BTC monitored at 443 nm under 77 K. The wavelength of the excitation was 300 nm in (a)-(d), and 350 nm in (e) and (f).

photodynamic therapy [49]. On the basis of the photoluminescence results discussed above, we expect that both Bi-TATB and Bi-BTC can induce the $^3O_2 \rightarrow {}^1O_2$ conversion (hereafter referred to as the activation of molecular oxygen). To investigate the nature of this activation of molecular oxygen, we first examine the oxidation of 3,3′,5,5′-tetramethylbenzidine (TMB) under UV-vis irradiation in the presence of Bi-TATB or Bi-BTC. As shown in Figure S8, the partially oxidized product of TMB can be monitored by studying its optical absorption at around 370 and 652 nm. As illustrated in Fig. 4a, the continuous increase in the absorption at 370 and 652 nm clearly indicates the photocatalytic oxidation of TMB molecules induced by Bi-TATB under UV–vis irradiation. To probe what species are needed for the TMB oxidation, we carried out experiments with Bi-TATB under different gases and monitored the oxidation results by examining the absorption peak at 370 nm. Fig. 4b shows that the amount of oxidation products under Ar is far less than those under air and $O_2$. This suggests that the active species for the TMB oxidation arises from the activation of molecular oxygen. We obtain similar results using Bi-BTC, namely, Bi-BTC can oxidize TMB molecules by the activation of oxygen molecules (Fig. 4c-d). According to the absorbance values, the amount of the oxidation products induced by Bi-BTC is smaller than that by Bi-TATB.

The reactive oxygen species (ROS) generated by the activation of molecular oxygen can be superoxide radical ($O_2^{\cdot -}$), hydroxyl radical ($^{\cdot}OH$), hydrogen peroxide ($H_2O_2$), and singlet oxygen ($^1O_2$). To identify which one of these species is involved, we carried out the TMB oxidation experiments in the presence of various scavengers, namely, superoxide dismutase (SOD) for superoxide radical ($O_2^{\cdot -}$), mannitol for hydroxyl radical ($^{\cdot}OH$), catalase for hydrogen peroxide ($H_2O_2$), and carotene for singlet oxygen ($^1O_2$). Fig. 4e shows that carotene suppresses the TMB oxidation by Bi-TATB (~29.25%), while other scavengers have negligible effects. This suggests that $^1O_2$ is the major photogenerated reactive oxygen species. For Bi-BTC (Fig. 4f), the inhibiting effect of carotene is much higher (~68.31%) showing that $^1O_2$ is the dominant photogenerated species. The TMB oxidation experiments

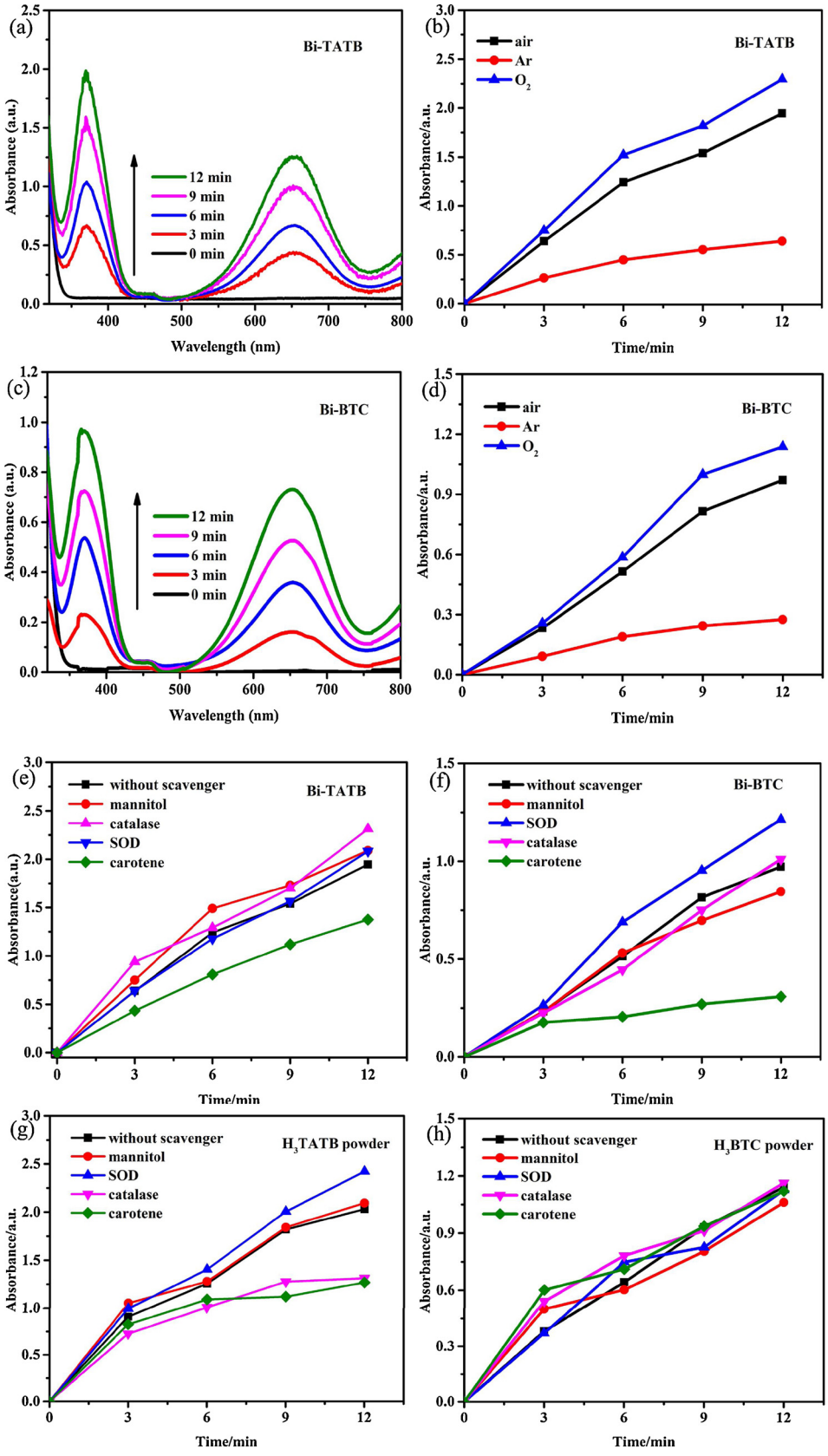


**Fig. 4.** (a) Evolution of the absorption spectra of TMB oxidation in the presence of Bi-TATB in air. (b) Absorbance evolution of TMB oxidation with Bi-TATB monitored at 370 nm under different gas conditions. (c) Evolution of the absorption spectra of TMB oxidation in the presence of Bi-BTC in air. (d) Absorbance evolution of TMB oxidation with Bi-BTC monitored at 370 nm under different gas conditions. (e) Absorbance of TMB oxidation with Bi-TATB monitored at 370 nm in the presence of different scavengers. (f) Absorbance of TMB oxidation with Bi-BTC monitored at 370 nm in the presence of different scavengers. (g) Absorbance of TMB oxidation with $H_3$TATB powder monitored at 370 nm in the presence of different scavengers. (h) Absorbance of TMB oxidation with $H_3$BTC powder monitored at 370 nm in the presence of different scavengers.

were also carried out in the presence of $H_3$TATB and $H_3$BTC powders using different scavengers (Fig. 4g, h). In the case of $H_3$TATB powder, both carotene and catalase suppress the TMB oxidation more effectively than the other scavengers, showing that both $^1O_2$ and $H_2O_2$ are the major oxidizing species (Fig. 4g). In the case of $H_3$BTC powder, all scavengers have a similar effect, showing that all oxidizing species are involved in the TMB oxidation (Fig. 4h). In addition, the TMB oxidation in the presence of $H_3$TATB monomers shows that all reactive oxygen

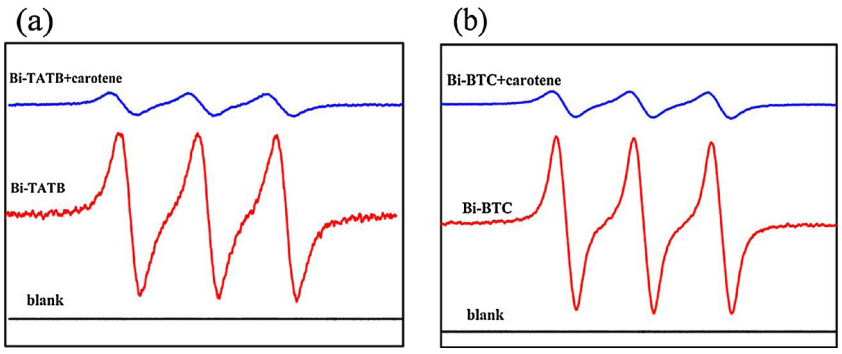


**Fig. 5.** ESR spectra for (a) Bi-TATB and (b) Bi-BTC samples with/without carotene in the presence of TEMP in acetone.

**Table 1**
Photo-Oxidation of Various Aromatic Alcohols over Bi-TATB and Bi-BTC.[a]

| Substrate | Bi-TATB | | | Bi-BTC | | |
|---|---|---|---|---|---|---|
| | Time[b] | Conversion[c] | Selectivity[c] | Time[b] | Conversion[c] | Selectivity[c] |
| 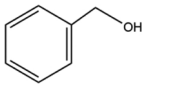 | 5 | 37.59 | 100 | 12 | 3.92 | 100 |
| 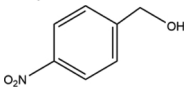 | 5 | 26.89 | 100 | 18 | 3.21 | 100 |
| 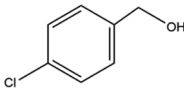 | 5 | 17.22 | 83.8 | 10 | 1.69 | 100 |
| 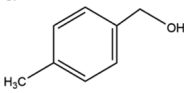 | 5 | 40.58 | 78 | 16 | 3.12 | 99.1 |

[a] Reaction conditions: catalyst (20 mg), alcohol (20 μmol), 20 mL of hexane, UV–vis light, $O_2$ bubble, temperature = 15 °C.
[b] Reaction time in hours.
[c] Selectivity and conversion are in mol %.

**Table 2**
Stability Test of Photo-Oxidation of Benzyl Alcohol over Bi-TATB and Bi-BTC.[a].

| Circulation Times | Bi-TATB | | | Bi-BTC | | |
|---|---|---|---|---|---|---|
| | Time[b] | Conversion[c] | Selectivity[c] | Time[b] | Conversion[c] | Selectivity[c] |
| Cycle 1 | 5 | 37.25 | 100.00 | 12 | 3.89 | 100 |
| Cycle 2 | 5 | 39.50 | 100.00 | 12 | 4.09 | 100 |
| Cycle 3 | 5 | 41.82 | 95.65 | 12 | 6.70 | 90.24 |
| Cycle 4 | 5 | 50.76 | 92.14 | 12 | 9.41 | 85.74 |

[a] Reaction conditions: catalyst (20 mg), alcohol (20 μmol), 20 mL of hexane, UV–vis light, $O_2$ bubble, temperature = 15 °C.
[b] Reaction time in hours.
[c] Selectivity and conversion are in mol %.

species play a role in the oxidation (Figure S9). To further verify that the presence of a heavy-atom such as Bi in MOFs can induce the $^3O_2 \rightarrow {}^1O_2$ conversion, we replace the Bi atom by Co atom to form a $Co_4O(TATB)_{8/3}$ MOFs [50], in which the organic ligand is still $TATB^{3-}$. The XRD patterns in Figure S10a confirm that it is synthesized successfully. The experiments to find reactive oxygen species (Figure S10b) in $Co_4O(TATB)_{8/3}$ MOFs were performed under the same conditions as described above, showing that both carotene and catalase can suppress the TMB oxidation. This result is similar to that for the $H_3TATB$ powder samples. Namely, in the absence of the heavy-atom effect, $^1O_2$ is not a dominant reactive oxygen species.

Electron spin resonance (ESR) measurements were carried out to gain more direct proofs for the photogenerated reactive oxygen species. 2,2,6,6-Tetramethylpiperidine (TEMP) is employed as the trapping agents for $^1O_2$, the oxidation process of which is shown in Figure S11. As illustrated in Fig. 5a, a 1:1:1 triplet signal with g-value of 2.0056 occurs in the presence of Bi-TATB, which can be indexed to the generation of 2,2,6,6-Tetramethylpiperidine-*N*-oxyl (TEMPO). In the presence of carotene, this signal is greatly suppressed, further indicating that the reactive oxygen species is $^1O_2$. For Bi-BTC, similar results are obtained (Fig. 5b). The other possible oxidant such as $O_2^{\cdot -}$, $^{\cdot}OH$ and $H_2O_2$ that may be formed during the photocatalytic process were further investigated using ESR spectra. As can be seen in Figure S12, the characteristic signal of $O_2^{\cdot -}$ and $H_2O_2$ can be found in the presence of organic ligand, i.e. $H_3TATB$ and $H_3BTC$. In contrast, no obvious signal can be detected under the same conditions when $H_3TATB$ and $H_3BTC$ are replaced by Bi-TATB and Bi-BTC. These results excludes the formation of $O_2^{\cdot -}$, $^{\cdot}OH$ and $H_2O_2$. The presence of Bi suppresses the

generation of $O_2^{\cdot -}$ and $H_2O_2$ and singlet oxygen $^1O_2$ is the only active oxygen product over Bi-TATB and Bi-BTC.

In view of the high selectivity and efficiency for $^1O_2$ generation, Bi-TATB and Bi-BTC are expected to be a promising photocatalyst for selective oxidation reactions involving $^1O_2$. We employ the selective alcohol oxidation reaction to aldehyde, to evaluate the photocatalytic performance of Bi-TATB and Bi-BTC,

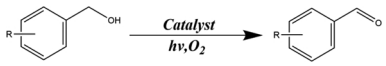


which has been widely studied due to the crucial role in the synthesis of fine chemicals and intermediates [51], to evaluate the photocatalytic performance of Bi-TATB and Bi-BTC. There are two issues to consider, i.e., selectivity and activity. The selectivity is measured by the ratio of the yield of aldehyde to the overall conversion of alcohol to all possible oxidized products. The activity of $^1O_2$ is the amount of aldehyde generated. Table 1 summarizes the conversion rate and selectivity for the oxidation of a series of alcohols. (The yields and identities of the oxidized products of alcohols were determined by gas chromatography as discussed in the supporting information).

For Bi-TATB, benzyl alcohol was partly oxidized with a conversion of 37.59% in 5 h, but the selectivity for aldehyde is close to 100%, namely, no other oxidized product such as carboxylic acid is found. The GC patterns of specific oxidation process are shown in Figure S13. The effect of substitutions on the aromatic ring was further studied. The selectivity is much higher for the electron withdrawing substituent (-$NO_2$ and -Cl) compared with the electron donating substituent ($-CH_3$). In contrast, the conversion efficiency increases with increasing the electron donating ability of the substituent. Under an inert atmosphere or in the absence of Bi-TATB, only a trace amount of products is obtained, suggesting that the presence of oxygen molecules and catalysts are both needed. In contrast, the selectivity of Bi-BTC is almost 100% regardless of the nature of the substituents on the aromatic ring. However, Bi-BTC leads to a very poor conversion rate even after a much longer reaction time. This means that, for Bi-BTC, the amount of $^1O_2$ produced in the photocatalytic process is much smaller than that for Bi-TATB.

It is of interest to consider why Bi-TATB and Bi-BTC are different in their selectivity and activity. Our ROS measurements (Fig. 4e-f) show that $^1O_2$ is a dominating species for Bi-BTC compared with other reactive species. A poor activity of Bi-BTC compared with that of Bi-TATB means that the quantity of $^1O_2$ generated by Bi-BTC is far smaller than that by Bi-TATB, only about a tenth. Why is there a large difference on the quantities of $^1O_2$ generated by the two Bi-MOFs? The probable reason can be as follows. First, compared with Bi-TATB, Bi-BTC has much smaller surface area (7.27 $m^2 g^{-1}$) than that of Bi-TATB (151.73 $m^2 g^{-1}$) as shown in Figure S14. Therefore, less active site for Bi-BTC are exposed to $^3O_2$ resulting in decreased generation of $^1O_2$. Second, Bi-TATB absorbs more photons than does Bi-BTC (Figure S5), so there are more excitons in the excited state of Bi-TATB. Last, the triplet excitons have a longer lifetime in Bi-TATB than in Bi-BTC (4.77 vs.2.87 ms), which means triplet excitons exist for a longer period of time in Bi-TATB and hence can convert more $^3O_2$ into $^1O_2$.

To check the stability of Bi-TATB and Bi-BTC, four cycles of photocatalytic oxidation were carried out using benzyl alcohol as a representative. As shown in Table 2, both Bi-TATB and Bi-BTC display a decrease in selectivity since the third cycle, however, the selectivity still remains at a high level, larger than 85%. Meanwhile, the conversion efficiency gradually increases from the third cycle, which means by-products start to be produced. The reason is due to the partial collapse of the MOFs framework structure, as indicated by the XRD patterns after the fourth cycle. (Figure S15) The main peaks of Bi-TATB and Bi-BTC are preserved, however, the peak intensity decreases to some extent. This result implies that part of the framework structure collapses under mechanical stirring. This further emphasize the significant role of Bi in promoting the formation of singlet oxygen and the resulting high selectivity of photo-oxidation of benzyl alcohol to aldehyde.

## 4. Conclusion

In summary, we examined the heavy-atom effect of the $Bi^{3+}$ cations in Bi-TATB and Bi-BTC on the singlet → triplet intersystem crossing of the excited states of their organic ligands $TATB^{3-}$ and $BTC^{3-}$. This intersystem crossing induces the $^3O_2$ → $^1O_2$ conversion, and the resulting singlet oxygen $^1O_2$ oxidizes benzyl alcohol to benzaldehyde with high selectivity and activity under UV–vis light irradiation in the presence of Bi-TATB. Compared with Bi-TATB, Bi-BTC has a poor activity because the amount of $^1O_2$ produced is much smaller for Bi-BTC than for Bi-TATB. Our work provides an alternative approach toward selective organic synthesis.

## Conflicts of interest

The authors declare no competing financial interest.

## Acknowledgement

This work was financially supported by the National Natural Science Foundation of China(No. 21333006, 21573135, U1832145, 11374190, 51321091 and 51602179), and Young Scholars Program (2016WLJH16).

## Appendix A. Supplementary data

Supplementary material related to this article can be found, in the online version, at doi:https://doi.org/10.1016/j.apcatb.2019.05.024.

## References

[1] K. Shimura, H. Yoshida, Heterogeneous photocatalytic hydrogen production from water and biomass derivatives, Energy Environ. Sci. 4 (2011) 2467–2481.
[2] Y.Q. Wu, P. Wang, X.L. Zhu, Q.Q. Zhang, Z.Y. Wang, Y.Y. Liu, G.Z. Zou, Y. Dai, M.H. Whangbo, B.B. Huang, Composite of $CH_3NH_3PbI_3$ with reduced graphene oxide as a highly efficient and stable visible-light photocatalyst for hydrogen evolution in aqueous HI solution, Adv. Mater. 30 (2018) 1704342.
[3] Y. An, Y.Y. Liu, P.F. An, J.C. Dong, B.Y. Xu, Y. Dai, X.Y. Qin, X.Y. Zhang, M.H. Whangbo, B.B. Huang, $Ni^{II}$ coordination to Al-based metal-organic framework made from 2-aminoterephthalate for photocatalytic overall water splitting, Angew. Chem. Int. Ed. 56 (2017) 3036–3040.
[4] Y.Q. Wu, P. Wang, Z.H. Guan, J.X. Liu, Z.Y. Wang, Z.K. Zheng, S.Y. Jin, Y. Dai, M.H. Whangbo, B.B. Huang, Enhancing the photocatalytic hydrogen evolution activity of mixed-halide perovskite $CH_3NH_3PbBr_3$-xIx achieved by bandgap funneling of charge carriers, ACS. Catal. 8 (2018) 10349.
[5] G.Z. Wang, Q.L. Sun, Y.Y. Liu, B.B. Huang, Y. Dai, X.Y. Zhang, X.Y. Qin, A bismuth-based metal-organic framework as an efficient visible-light-driven photocatalyst, Chem.-Eur. J. 21 (2015) 2364–2367.
[6] C.C. Wang, J.R. Li, X.L. Lv, Y.Q. Zhang, Photocatalytic organic pollutants degradation in metal-organic frameworks, Energy Environ. Sci. 7 (2014) 2831–2867.
[7] J. Medina-Ramos, J.L. DiMeglio, J. Rosenthal, Efficient reduction of $CO_2$ to CO with high current density using in situ or ex situ prepared Bi-based materials, J. Am. Chem. Soc. 136 (2014) 8361–8367.
[8] A.V. Akimov, R. Asahi, R. Jinnouchi, O.V. Prezhdo, What makes the photocatalytic $CO_2$ reduction on N-doped $Ta_2O_5$ efficient: insights from nonadiabatic molecular dynamics, J. Am. Chem. Soc. 137 (2015) 11517–11525.
[9] N. Corrigan, S. Shanmugam, J.T. Xu, C. Boyer, Photocatalysis in organic and polymer synthesis, Chem. Soc. Rev. 45 (2016) 6165–6212.
[10] A.A. High, E.E. Novitskaya, L.V. Butov, M. Hanson, A.C. Gossard, Control of exciton fluxes in an excitonic integrated circuit, Science 321 (2008) 229–231.
[11] Y.L. Chang, Y.L. Rao, S.L. Gong, G.L. Ingram, S.N. Wang, Z.H. Lu, Exciton-stimulated molecular transformation in organic light-emitting diodes, Adv. Mater. 26 (2014) 6729–6733.
[12] V. Sukhovatkin, S. Hinds, L. Brzozowski, E.H. Sargent, Colloidal quantum-dot photodetectors exploiting multiexciton generation, Science 324 (2009) 1542–1544.
[13] J.B. Sambur, T. Novet, B.A. Parkinson, Multiple exciton collection in a sensitized photovoltaic system, Science 330 (2010) 63–66.
[14] J.H. Werner, S. Kolodinski, H.J. Queisser, Novel optimization principles and efficiency limits for semiconductor solar-sells, Phys. Rev. Lett. 72 (1994) 3851–3854.
[15] H. Wang, S.L. Jiang, W. Shao, X.D. Zhang, S.C. Chen, X.S. Sun, Q. Zhang, Y. Luo, Y. Xie, Optically switchable photocatalysis in ultrathin black phosphorus

nanosheets, J. Am. Chem. Soc. 140 (2018) 3474–3480.
[16] H. Wang, S.L. Jiang, S.C. Chen, X.D. Zhang, W. Shao, X.S. Sun, Z. Zhao, Q. Zhang, Y. Luo, Y. Xie, Insights into the excitonic processes in polymeric photocatalysts, Chem. Sci. 8 (2017) 4087–4092.
[17] Y. Bai, X. Shi, P.Q. Wang, H.Q. Xie, L.Q. Ye, Photocatalytic mechanism regulation of bismuth oxyhalogen via changing atomic assembly method, ACS Appl. Mater. Interfaces 9 (2017) 30273–30277.
[18] H. Wang, D.Y. Yong, S.C. Chen, S.L. Jiang, X.D. Zhang, W. Shao, Q. Zhang, W.S. Yan, B.C. Pan, Y. Xie, Oxygen-vacancy-mediated exciton dissociation in BiOBr for boosting charge-carrier-involved molecular oxygen activation, J. Am. Chem. Soc. 140 (2018) 1760–1766.
[19] H. Wang, X.S. Sun, D.D. Li, X.D. Zhang, S.C. Chen, W. Shao, Y.P. Tian, Y. Xie, Boosting hot-electron generation: exciton dissociation at the order disorder interfaces in polymeric photocatalysts, J. Am. Chem. Soc. 139 (2017) 2468–2473.
[20] H. Wang, S.C. Chen, D.Y. Yong, X.D. Zhang, S. Li, W. Shao, X.S. Sun, B.C. Pan, Y. Xie, Giant electron-hole interactions in confined layered structures for molecular oxygen activation, J. Am. Chem. Soc. 139 (2017) 4737–4742.
[21] M.C. DeRosa, R.J. Crutchley, Photosensitized singlet oxygen and its applications, Coordin. Chem. Rev. 233 (2002) 351–371.
[22] P.V. Lakshmi, V. Rajagopalan, A new synergetic nanocomposite for dye degradation in dark and light, Sci. Rep.-Uk 6 (2016) 38606.
[23] S. Talukdar, R.K. Dutta, A mechanistic approach for superoxide radicals and singlet oxygen mediated enhanced photocatalytic dye degradation by selenium doped ZnS nanoparticles, Rsc. Adv. 6 (2016) 928–936.
[24] S. Ballut, D. Naud-Martin, B. Loock, P. Maillard, A strategy for the targeting of photosensitizers. Synthesis, characterization, and photobiological property of porphyrins bearing glycodendrimeric moieties, J. Org. Chem. 76 (2011) 2010–2028.
[25] M.R. Ke, S.L. Yeung, W.P. Fong, D.K.P. Ng, P.C. Lo, A phthalocyanine-peptide conjugate with high in vitro photodynamic activity and enhanced in vivo tumor-retention property, Chem.-Eur. J. 18 (2012) 4225–4233.
[26] A. Gorman, J. Killoran, C. O'Shea, T. Kenna, W.M. Gallagher, D.F. O'Shea, In vitro demonstration of the heavy-atom effect for photodynamic therapy, J. Am. Chem. Soc. 126 (2004) 10619–10631.
[27] L.M. Rossi, P.R. Silva, L.L.R. Vono, A.U. Fernandes, D.B. Tada, M.S. Baptista, Protoporphyrin IX nanoparticle carrier: preparation, optical properties, and singlet oxygen generation, Langmuir 24 (2008) 12534–12538.
[28] Q.A. Zhao, F.Y. Li, C.H. Huang, Phosphorescent chemosensors based on heavy-metal complexes, Chem. Soc. Rev. 39 (2010) 3007–3030.
[29] L.Y. Cao, Z.K. Lin, W.J. Shi, Z. Wang, C.K. Zhang, X.F. Hu, C. Wang, W.B. Lin, Exciton migration and amplified quenching on two-dimensional metal-organic layers, J. Am. Chem. Soc. 139 (2017) 7020–7029.
[30] H.J. Son, S.Y. Jin, S. Patwardhan, S.J. Wezenberg, N.C. Jeong, M. So, C.E. Wilmer, A.A. Sarjeant, G.C. Schatz, R.Q. Snurr, O.K. Farha, G.P. Wiederrecht, J.T. Hupp, Light-harvesting and ultrafast energy migration in porphyrin-based metal-organic frameworks, J. Am. Chem. Soc. 135 (2013) 862–869.
[31] C.A. Kent, D. Liu, T.J. Meyer, W. Lin, Amplified luminescence quenching of phosphorescent metal-organic frameworks, J. Am. Chem. Soc. 134 (2012) 3991–3994.
[32] A.N. Meng, L.X. Chaihu, H.H. Chen, Z.Y. Gu, Ultrahigh adsorption and singlet-oxygen mediated degradation for efficient synergetic removal of bisphenol A by a stable zirconiumporphyrin metal-organic framework, Sci. Rep.-Uk 7 (2017) 6297.
[33] Z.X. Chen, M.D. Liu, M.K. Zhang, S.B. Wang, L. Xu, C.X. Li, F. Gao, B.R. Xie, Z.L. Zhong, X.Z. Zhang, Interfering with lactate-fueled respiration for enhanced photodynamic tumor therapy by a porphyrinic MOF nanoplatform, Adv. Funct. Mater. 28 (2018) 1803498.
[34] K. Zhang, X.D. Meng, Y. Cao, Z. Yang, H.F. Dong, Y.D. Zhang, H.T. Lu, Z.J. Shi, X.J. Zhang, Metal-organic framework nanoshuttle for synergistic photodynamic and low-temperature photothermal therapy, Adv. Funct. Mater. 28 (2018) 1804634.
[35] K.D. Lu, C.B. He, W.B. Lin, Nanoscale metal-organic framework for highly effective photodynamic therapy of resistant head and neck cancer, J. Am. Chem. Soc. 136 (2014) 16712–16715.
[36] K.D. Lu, C.B. He, N.N. Guo, C. Chan, K.Y. Ni, R.R. Weichselbaum, W.B. Lin, Chlorin-based nanoscale metal-organic framework systemically rejects colorectal cancers via synergistic photodynamic therapy and checkpoint blockade immunotherapy, J. Am. Chem. Soc. 138 (2016) 12502–12510.
[37] Y.W. Zhao, Y. Kuang, M. Liu, J. Wang, R.J. Pei, Synthesis of metal-organic framework nanosheets with high relaxation rate and singlet oxygen yield, Chem. Mater. 30 (2018) 7511–7520.
[38] A. Balamurugan, A.K. Gupta, R. Boomishankar, M.L. Reddy, M. Jayakannan, Heavy atom effect driven organic phosphors and their luminescent lanthanide metal-organic frameworks, Chempluschem 78 (2013) 737–745.
[39] G.Z. Wang, Y.Y. Liu, B.B. Huang, X.Y. Qin, X.Y. Zhang, Y. Dai, A novel metal-organic framework based on bismuth and trimesic acid: synthesis, structure and properties, Dalton T. 44 (2015) 16238–16241.
[40] M. Koppen, O. Beyer, S. Wuttke, U. Luning, N. Stock, Synthesis, functionalisation and post-synthetic modification of bismuth metal-organic frameworks, Dalton T. 46 (2017) 8658–8663.
[41] S.O. Kim, T.K. An, J. Chen, I. Kang, S.H. Kang, D.S. Chung, C.E. Park, Y.H. Kim, S.K. Kwon, H-aggregation strategy in the design of molecular semiconductors for highly reliable organic thin film transistors, Adv. Funct. Mater. 21 (2011) 1616–1623.
[42] J.R. Yu, J.H. Park, A.V. Wyk, G. Rumbles, P. Deria, Excited-state electronic properties in Zr-based metal-organic frameworks as a function of a topological network, J. Am. Chem. Soc. 140 (2018) 10488–10496.
[43] M.A. Nasalevich, C.H. Hendon, J.G. Santaclara, K. Svane, B. Linden, S.L. Veber, M.V. Fedin, A.J. Houtepen, M.A. van der Veen, F. Kapteijn, A. Walsh, J. Gascon, Electronic origins of photocatalytic activity in $d^0$ metal organic frameworks, Sci. Rep.-Uk 6 (2016) 23676.
[44] Y.V. Romanovskii, A. Gerhard, B. Schweitzer, U. Scherf, R.I. Personov, H. Bassler, Phosphorescence of pi-conjugated oligomers and polymers, Phys. Rev. Lett. 84 (2000) 1027–1030.
[45] P.R. Ogilby, Singlet oxygen: there is indeed something new under the sun, Chem. Soc. Rev. 39 (2010) 3181–3209.
[46] T. Montagnon, M. Tofi, G. Vassilikogiannakis, Using singlet oxygen to synthesize polyoxygenated natural products from Furans, Accounts. Chem. Res. 41 (2008) 1001–1011.
[47] X. Ragas, A. Jimenez-Banzo, D. Sanchez-Garcia, X. Batllori, S. Nonell, Singlet oxygen photosensitisation by the fluorescent probe singlet oxygen sensor green®, Chem. Commun. (2009) 2920–2922.
[48] D. Kovalev, M. Fujii, Silicon nanocrystals: photosensitizers for oxygen molecules, Adv. Mater. 17 (2005) 2531–2544.
[49] K. Ishii, Functional singlet oxygen generators based on phthalocyanines, Coordin. Chem. Rev. 256 (2012) 1556–1568.
[50] S.Q. Ma, D.Q. Yuan, J.S. Jong-San Chang, H.C. Zhou, Investigation of gas adsorption performances and $H_2$ affinities of porous metal-organic frameworks with different entatic metal centers, Inorg. Chem. 48 (2009) 5398–5402.
[51] Y.Z. Chen, Z.U. Wang, H.W. Wang, J.L. Lu, S.H. Yu, H.L. Jiang, Singlet oxygen-engaged selective photo-oxidation over Pt nanocrystals/porphyrinic MOF: The roles of photothermal effect and Pt electronic state, J. Am. Chem. Soc. 139 (2017) 2035–2044.